China Instrument and Control Society
Instrumentation
INSTRUMENTATION, Vol. 11, No. 2, June 2024 https://doi.org/10.15878/j.instr.202400029

Article

Automatic Monitoring System for 3-D Deformation of Crustal Fault Based on Laser and Machine Vision

Qingshan Wang, Guoying Su*, Qingzun Ma, Haiquan Yin, Zhihang Liu, Chuanzhen Lv

The First Monitoring and Application Center, China Earthquake Administration, Tianjin 300180

* Corresponding author email: suying913824@163.com

Abstract: An automatic monitoring method of the 3-D deformation is presented for crustal fault based on laser and machine vision. The laser source and screen are independently set up in the headwall and footwall, the collimated laser beam creates a circular spot on the screen, meanwhile, the industrial camera captures the tiny deformation of the crustal fault by monitoring the change of the spot position. This method significantly reduces the cost of equipment and labor, provides daily sampling to ensure high continuity of data. A prototype of the automatic monitoring system is developed, and a repeatability test indicates that the error of spot jitter can be minimized by consecutive samples. Meanwhile, the environmental correction model is determined to ensure that environmental changes do not disturb the system. Furthermore, the automatic monitoring system has been applied at the deformation monitoring station (KJX02) of China Beishan underground research laboratory, where continuous deformation monitoring is underway.

Keywords: deformation measurement; crustal fault; automatic monitoring; laser spot; machine vision

Citation: Qingshan Wang, Guoying Su, Qingzun Ma, Haiquan Yin, Zhihang Liu, and Chuanzhen Lu. "Automatic Monitoring System for 3-D Deformation of Crustal Fault Based on Laser and Machine Vision." Instrumentation 11, no. 2 (2024). https://doi.org/10.15878/j.instr.202400029.

1 Introduction

Under the action of tectonic stresses, the crust will deform slightly in vertical, horizontal, or inclined directions, numerous researches indicate that strain rate field analysis, inversion of fault locking and the velocity profiles analysis[1] based on deformation monitoring data have become the essential foundation for crustal movement and earthquake forecasting research. For instance, the deep structure and surface deformation of the crust in the northeastern Tibetan Plateau are revealed to investigate the mechanism of growth and expansion based on gravity changes and 3-D crustal deformations dataset[2]; the strain state in Tohoku-Oki region of Japan before the Mw 9.0 mainshock is significantly different from that in the interseismic period in terms of principal strain rate and direction of motion[3]; additionally, eastward velocity surrounding the epicenter experienced a significant decrease over two and a half years before the Mw 6.7 Lushan earthquake in China, meanwhile, the eastward velocity at each global positioning system station is increasingly reduced with increasing proximity to the epicenter[4]; Thus, the analysis of time-series on crustal deformation has great significance in promoting disaster prevention.

A range of effective and unique instruments have emerged to meet the monitoring requirements for crustal deformations. The precision level is an essential tool for geodetic elevation surveys and is used for high-precision deformation measurements in vertical direction[5]. Interferometric synthetic aperture radar (InSAR) allows for by measuring active surface deformation by repeat-pass differential radar interferometry[6]. As the basis for analyzing of crustal movement and monitoring efforts, the global navigation satellite system (GNSS) achieves large-scale deformation measurement with high automation and excellent horizontal resolution[7], but limited precision in the vertical direction. As a popular

and leading geodetic tool, the total station is used for deformation monitoring in short-baseline situations by obtaining distances, angles and 3-D coordinates of points[8].

In addition, more advanced deformation monitoring methods are being explored to overcome certain engineering challenges. Robotic total stations are equipped with servomotors to drive both horizontal and vertical motions with automatic search for prism targets, which improved measurement efficiency and deployed in subway tunnels in Hong Kong[9]. With low cost, short revisiting cycle, flexibility and high precision, aerial photogrammetry has been developed for terrain surveying[10], which was designed to determine vertical deformation from differences in digital surface models created by unmanned aerial vehicles equipped with digital camera, and horizontal deformation from points of observation lines and scattered situational details[11]. Combined with laser level deformation monitor and weak fiber Bragg grating, a multi-layer intelligent monitoring system was developed to comprehensively monitor tunnel inverted arch filling and internal deformation[12]. The multipurpose instrumental system provided continuous geomechanical monitoring of the pitwall by determining the accumulation level of deformation in rock mass[13].

On the whole, conventional geodetic methods have certain limitations, for example, the lack of automation in monitoring instruments leads to large labor costs, deformation monitoring by level and total station requires the cooperation of several people to be carried out properly, moreover, 3-D deformations are not usually available directly, but calculated by combining level, GNSS, total station or InSAR datasets[2,14]. Thus, this paper proposes a low cost automatic deformation monitoring technique for faults zones, and performs the design, construction and evaluation of an automatic monitoring system for 3-D deformation based on laser and machine vision.

2 Principles and structure of system

2.1 Deformation monitoring technology based on laser and machine vision

The deformation monitoring technology consists of collimated laser and machine vision, as visualized in Fig.1. Concrete pillar monuments are respectively installed on the solid bedrock in the headwall and footwall, where collimated laser and industrial camera are deployed. The collimated beam of laser passes through two optical windows and creates a circular spot on the screen in front of the industrial camera, which captures the tiny deformation of the crustal fault by monitoring the change of the spot position on the screen. XYZ-Axis linear stage is designed to determine the mathematical model for 3-D deformation measurement; Optical windows are designed from K9 glass[15] with high transmittance and excellent resistance to laser damage, furthermore, all components are placed in airtight containers made of stainless steel to avoid environmental influences.

2.2 Principle of 3-D deformation measurement method

The single-channel system can only acquire the deformation in the direction perpendicular to the laser beam, but not in the direction parallel to the laser beam, therefore, the dual-channel program is the minimum system to achieve 3-D deformation monitoring, as shown in Fig.2, where two collimated laser sources are placed on the same block of crustal fault, and the relative deformation of crustal fault is calculated by analyzing the displacement of the spot on both screens.

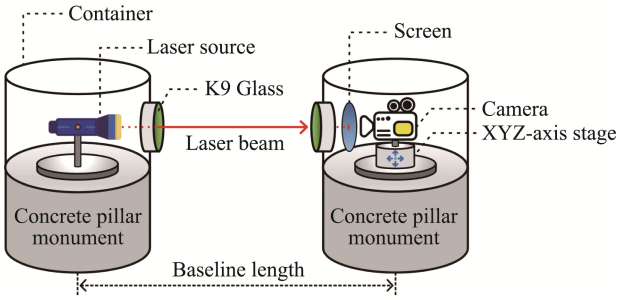

Fig.1 Schematic of deformation monitoring technology

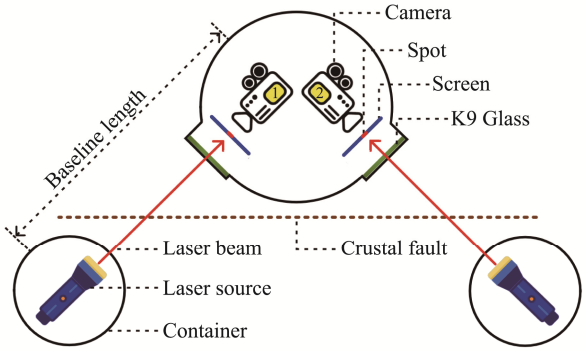

Fig.2 Dual-channel measurement schematic

In the deformation on a horizontal plane, if the movement is parallel to the crustal fault, as shown in Fig.3(a), the change of the abscissa of the spot position on both screens towards the same direction; if the movement is perpendicular to the crustal fault, as shown in Fig.3(b), the change of the abscissa of the spot position on both screens is opposite. In the deformation perpendicular to horizontal plane, the change of the ordinate of the spot position on both screens is the same.

Assuming that the angles between laser beams and the crustal fault are θ and φ, the deformations parallel and perpendicular to the crustal fault on the horizontal plane are x and y, and the deformation perpendicular to horizontal plane is z. The earth crust moves in the direction indicated in Fig.3, which contributes to a

consequent change in the spot position. The abscissa changes of two spots are Δx_1 and Δx_2, and the ordinate changes are Δy_1 and Δy_2, which can be calculated by image processing, the ideal mathematical model of the 3-D deformation measurement can be expressed as:

$$\begin{cases} \Delta x_1 = x \cdot sin\theta - y \cdot cos\theta \\ \Delta x_2 = x \cdot sin\varphi + y \cdot cos\varphi \\ \Delta y_1 + \Delta y_2 = 2 \cdot z \end{cases} \quad (1)$$

In field application, there is a height difference between concrete pillar monuments, thus, the laser beam is no longer perpendicular to the screen plane, which shifts the ordinate of the spot slightly when the distance between the laser source and screen changes, as shown in Fig.4.

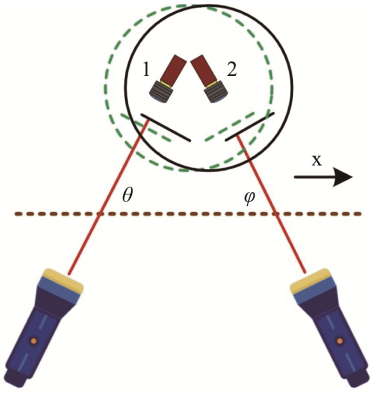

(a) Movement Parallel to the Fault

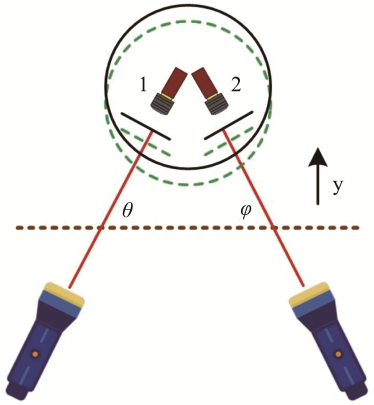

(b) Movement Perpendicular to the Fault

Fig.3 Crustal Fault movement leads to change in spot position (Green dotted line represents the original position, black solid line represents the position after moving)

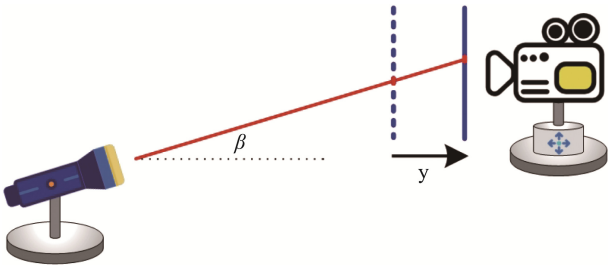

Fig.4 The offset of spot position caused by height difference between the concrete pillar monuments

Assuming that the angle between the laser beam and the horizontal plane is β, the mathematical model can be modified as:

$$\begin{cases} \Delta x_1 = x \cdot sin\theta - y \cdot cos\theta \\ \Delta x_2 = x \cdot sin\varphi + y \cdot cos\varphi \\ \Delta y_1 = z + (y \cdot sin\theta + x \cdot cos\theta) \cdot tan\beta \\ \Delta y_2 = z + (y \cdot sin\varphi - x \cdot cos\varphi) \cdot tan\beta \end{cases} \quad (2)$$

After concrete pillar monuments are poured, the angle of θ, φ and β can be measured by the total station to determine the mathematical model for 3-D deformation measurement. Moreover, the angle of θ, φ and β can also be obtained by system calibration: the X-axis (x_1, $x_2 \ldots x_n$), Y-axis (y_1, $y_2 \ldots y_n$) and Z-axis (z_1, $z_2 \ldots z_n$) were independently shifted multiple times with the other two axes fixed. Meanwhile, the offset data of spot positions were subsequently recorded, ultimately, the angle of θ, φ and β can be solved based on the least squares method.

2.3 Image processing and spot position calculation method

Although the brightness of the spot created by the laser beam on the screen is high, there is strong diffraction at the edges; therefore, image denoising and thresholding operations are necessary to improve the resolution of the spot position. Assume that the spot image is an $M \times N$ matrix, if the grayscale value $f(x, y)$ is lower than *thresh* set by users, the grayscale value of new pixel will be set to 0, which can be expressed as:

$$F(x,y) = \begin{cases} f(x,y), & f(x,y) \geq thresh \\ 0, & f(x,y) < thresh \end{cases} \quad (3)$$

Where x=1,2,3,3...M, y=1,2,3,...N, $F(x, y)$ denotes the grayscale distribution of images after the thresholding operation.

The shape and geometric center of the spot will be affected by the atmospheric turbulence instability and the aberration of the optical system, which makes the energy center of the spot deviate from the geometric center, therefore, the energy center calculated by weighting algorithm is considered as the true position of the spot, which can be expressed as:

$$\bar{x} = \frac{\sum_{x=1}^{M}\sum_{y=1}^{N} x \cdot F(x,y)}{\sum_{x=1}^{M}\sum_{y=1}^{N} F(x,y)} \quad \bar{y} = \frac{\sum_{x=1}^{M}\sum_{y=1}^{N} y \cdot F(x,y)}{\sum_{x=1}^{M}\sum_{y=1}^{N} F(x,y)} \quad (4)$$

Where $(\bar{x}, \bar{y})$ denotes the coordinate of the center of mass of the energy distribution. Fig.5 shows the image of the spot after non-local means denoising[16] and thresholding operation, with the red dot indicating the spot position. The noise in the spot area is significantly reduced and the edges of the spot are sharper.

2.4 Development of automatic monitoring system

The automatic monitoring system consists of the solar photovoltaic system, laser source control, image capture, weather observation, GNSS time service and graphical user interface, as illustrated in Fig.6. The solar photovoltaic system provides a stable 12V DC power to

ensure continuous operation of the unattended automatic monitoring system. The red dot laser source from LASEVER[17], with wavelength of 660 nm and output power of 200 mW, is controlled by serial port relay. The mono industrial camera (MV-CS050-10GM) from HIKROBOT[18], with SONY 2/3" IMX264 and resolution of 2448×2048, captures the image of the spot via Gigabit Ethernet. In addition, a weather sensor is incorporated into the system to measure various environmental parameters such as temperature, humidity, rainfall, illumination, atmospheric pressure, wind speed, and direction. Since deformation monitoring is usually performed in uninhabited area, the absence of network connectivity results in system clock drift, GNSS time service is used to coordinate the clock of industrial computers with an accuracy of 1μs.

The physical figure of the automatic monitoring system as shown in Fig.7, the desiccant was added to the container to prevent condensation on the optical window due to the diurnal temperature range, the container and the internal components are independent of each other to avoid instability of the spot position due to container vibration caused by environmental factors.

The automatic monitoring software was developed for human-computer interaction based on Python and Qt Designer, as shown in Fig.8, including measurement calibration, system control, communication setup, image analysis, data presentation, and operation log. The software supports daily sampling (at *hh:mm*) and continuous sampling (interval *n* minute) modes, and each sampling is performed as a high-speed multi-frame sample (max. frame rate 24.2 FPS), which reduces the random errors. The variation curves of the spot position are shown in '*L-Spot*" and '*R-Spot*" modules, which can be combined with the mathematical model to determine the 3-D deformation.

Featuring low cost, low electricity consumption, and high data continuity, the system achieves unmanned, automatic, and continuous deformation monitoring, the workflow is shown in Fig.9. Firstly, the mathematical model should be built, otherwise the crustal deformation cannot be calculated and only the change of spot position can be monitored. Secondly, the sampling mode,

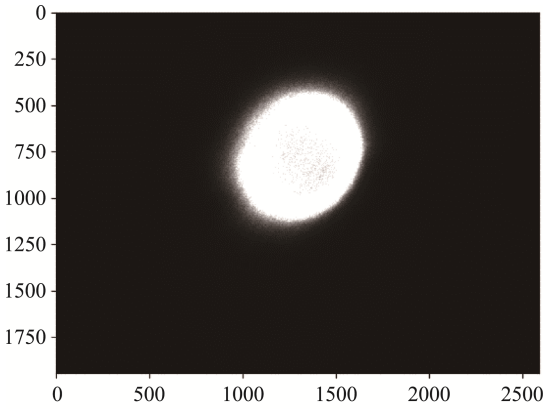

(a) Original image

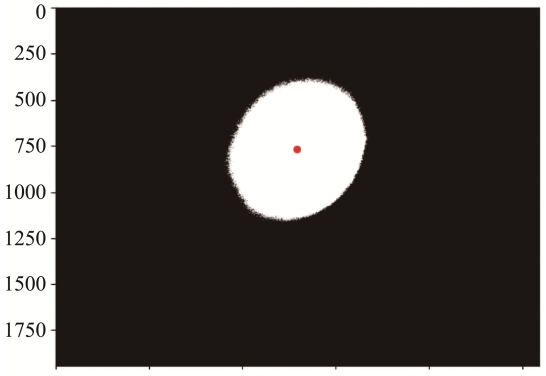

(b) Processed image

Fig.5 Comparison of original and processed image

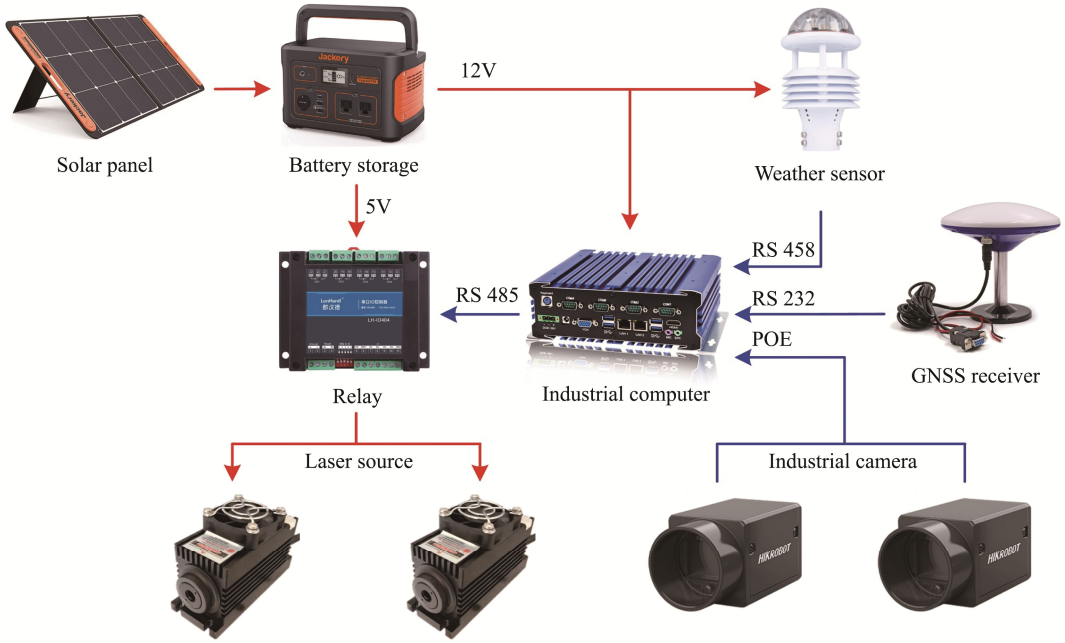

Fig.6 System functional framework

(a) Image capture sub-system at site W

(b) Laser source sub-system at site E

(c) The inside of image capture sub-system

(d) The inside of laser source sub-system

Fig.7 Automatic monitoring system at station KJX02

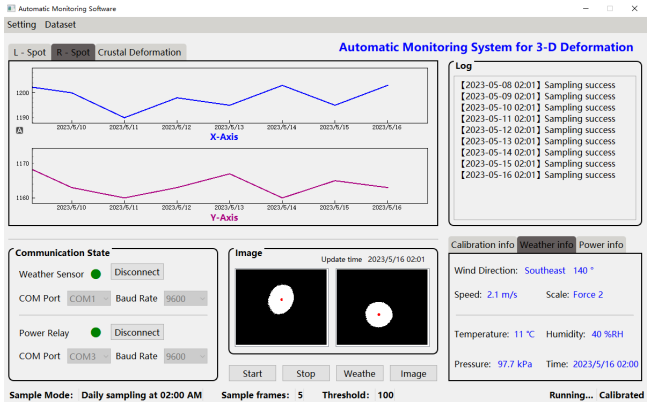

Fig.8 Automatic monitoring software
(Copyright registration number 2023SR0427750)

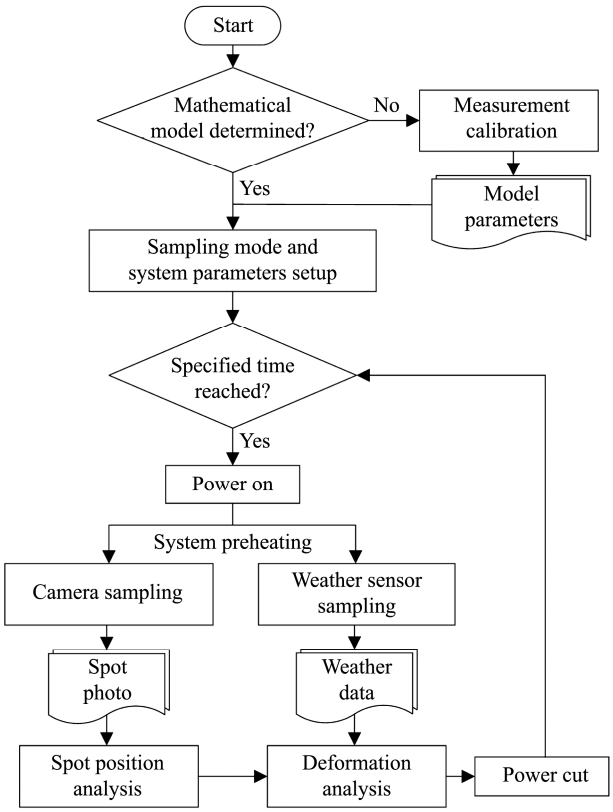

Fig.9 System flowchart

sampling frame, and image processing threshold should be configured. Finally, the system only samples at the time specified by the user during the automatic monitoring, therefore, it has extremely low deficient electricity consumption, and enables long-term continuous observation with solar photovoltaic system, which is suitable for application in depopulated zone to reduce monitoring cost.

3 System test and discussion

3.1 Repeatability test

Due to the uneven optical path of the laser, the spot will be slightly jittered on the screen. To evaluate the reliability and credibility of the measurement results, the repeatability test was carried out at night to avoid the effect of sunlight. The spot position was recorded at the sampling rate of 10 FPS for 40 times with 13 meters baseline, as shown in Fig.10.

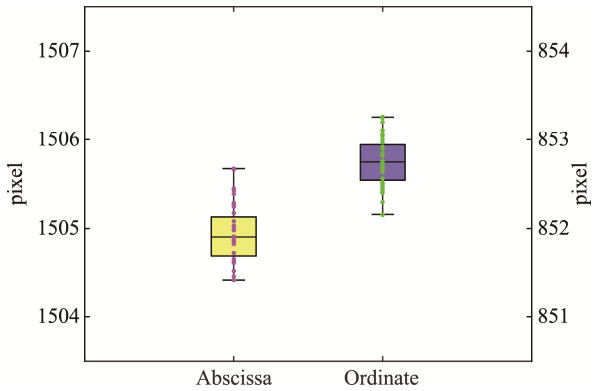

Fig.10 The distribution of spot position

The mean position of the spot is (1504.9379, 852.7606), the coordinate drift is lower than ±1 pixel, and the standard deviation (σ) was utilized for the stability test, which was calculated as follows:

$$\sigma = \sqrt{\frac{1}{n-1} \cdot \sum_{i=1}^{n} (N_i - \bar{N})^2} \tag{5}$$

Where n denotes the total number of samples, N_i denotes the measured value, and $\bar{N}$ denotes the sample mean. The standard deviation (σ) of abscissa is 0.2909,

and the ordinate is 0.2525. All the measured value conforms $N_i \in [\bar{N} \pm 2\sigma]$, which indicates that the data in this repeatability test are within the allowable range of error. Systems can generally be considered stable when the proportion of measured values within one standard deviation is more than 60%, in this test, the number of abscissas that conform to $N_i \in [\bar{N} \pm \sigma]$ is 25 (62.5 %) and ordinates is 26 (65 %), therefore, the system has great measurement stability and the negative effect of spot jitter can be minimized by calculating the mean value of multiple consecutive samples.

3.2 Environmental correction test

Under the influence of temperature and sunlight, there is thermal expansion of solids, which will lead to a small offset of spot position, and specific model should correct such environmental error. The environmental data collected through the weather sensor is the basis for the correction and the test was conducted at the test station shown in Fig.11, where concrete pillar monuments shared a common foundation and their respective positions were kept fixed, the offset of spot position was completely contributed by environmental factors. The host and image capture sub-system were installed at site *S*, and two laser source sub-systems were installed at sites *W* and *E*. The automatic monitoring system was configured to sample from 5:50 p.m. at an interval of 30 min, and 26 sets of spot positions and weather data were collected for the environmental correction test.

Since the variation of atmospheric pressure is extremely small, this section only explores the relationship between temperature, humidity and the offset of spot position. The binary linear regression analysis is performed for the abscissa and ordinate of the two spot positions based on regress toolbox in MATLAB, as shown in Fig.12.

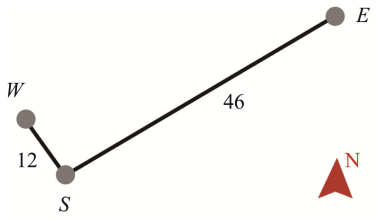

Fig.11 The site distribution of test station (Unit: m)

The r-squared statistics of the regression analysis shown in Fig.12(a), (b) and (c) are all above 0.97, which indicates the high reliability of the environmental correction model. However, Fig.12(d) shows that the ordinate of spot belongs to the interval (789,793) with the range of only 4 pixels, and such slight fluctuation was caused by atmospheric turbulence instability rather than by temperature and humidity variations, as evidenced by the low r-squared statistic of the regression analysis in Fig.12(d), thus, the temperature and humidity correction is not necessary for Fig.12(d).

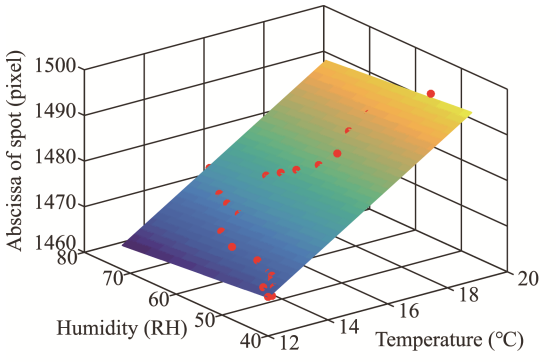

(a) The X-axis of the Left Image
(r^2=0.99; F=2068.96; $prob$=1.09*10^{-26}; s^2=0.40)

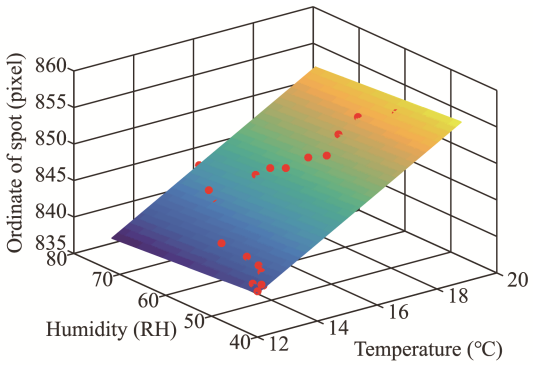

(b) The Y-axis of the Left Image
(r^2=0.97; F=415.57; $prob$=8.86*10^{-19}; s^2=0.63)

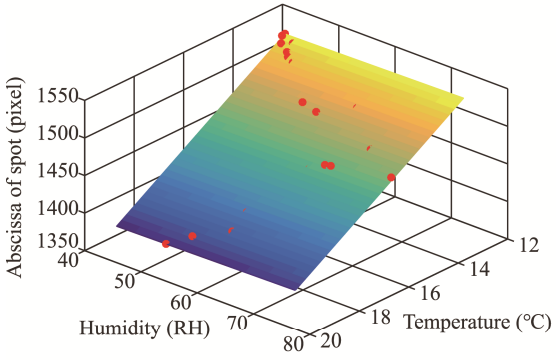

(c) The X-axis of the Right Image
(r^2=0.99; F=2427.64; $prob$=1.76; s^2=9.60)

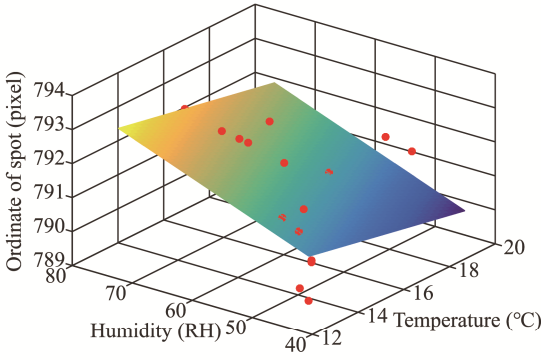

(d) The Y-axis of the Right Image
(r^2=0.2696; F=4.2440; $prob$=0.0270; s^2=0.7869)

Fig.12 Regression analysis of spot positions with temperature and humidity (r^2 is the r-squared statistic, F is the F-statistic, $prob$ is the p-value of the F-statistic, s^2 is the estimator of error variance)

The regression equation with temperature T and humidity RH as independent variables can be expressed as:

$$\begin{cases} f_a(T,RH)=1420.37+4.19\cdot T-0.10\cdot RH \\ f_b(T,RH)=813.81+2.34\cdot T-0.05\cdot RH \\ f_c(T,RH)=1776.19-21.60\cdot T+0.12\cdot RH \end{cases} \quad (6)$$

Eq. (6) shows that temperature has a more substantial influence on the offset of spot position than humidity. Combined with the regression equation, the environmental correction model can be built as:

$$Y_c=Y_r+Y_o-f(T, RH) \quad (7)$$

where Y_c is the corrected data, Y_r is the raw data, Y_o is the initial data at the first measurement and $f(T, RH)$ is the environmental correction function. The results of the environmental correction test are shown in Fig.13, the corrected data appear more stable and independent of changes in temperature and humidity, and still fluctuates within a small scale. The environmental correction test should be executed before the automatic monitoring system is officially run at each new station.

3.3 Application in Beishan underground research laboratory

Beishan Underground Research Laboratory (URL) is the first underground laboratory for Geological disposal of high-level radioactive waste in China[19,20], which consists of a shaft, three intersecting tunnels and two horizontal drifts at depths of –280 m and –560 m[21,22]. Commissioned by Beijing Research Institute of Uranium Geology, several deformation monitoring stations were set up around the Beishan URL to explore the geological effect of the deep excavation during the construction and to ensure the safety of geological disposal of radioactive waste, as shown in Fig.14.

According to the geological reconnaissance, *KJX02* was considered a suitable station for automatic monitoring system, which is located at the foot of the mountain with no outside road connection and has less possibility of human intervention than *KJX01* and *KJX03*. There are four monitoring sites (*W*, *N*, *S*, *E*) at *KJX02*, and each consisting of a high concrete pillar monument and a low concrete pillar monument with a common foundation, the high concrete pillar monument is used for levelling and laser distance measurement, the low concrete pillar monument is designed for an automatic monitoring system. According to the "Specifications for Cross-fault Geodetic Measurements" issued by China Earthquake Administration, the distance between monitoring sites was measured by precision baseline measurement through *Leica Nova TS60 Total Station*, the site distribution of *KJX02* is shown in Fig.15.

The host and image capture sub-system were installed at site *W*, and two laser source sub-systems were installed at site *S* and *E* to monitor the activity of *Jiujing* Fault, the automatic monitoring system is set to work at 2:00 a.m. every day with 30 frames per sampling.

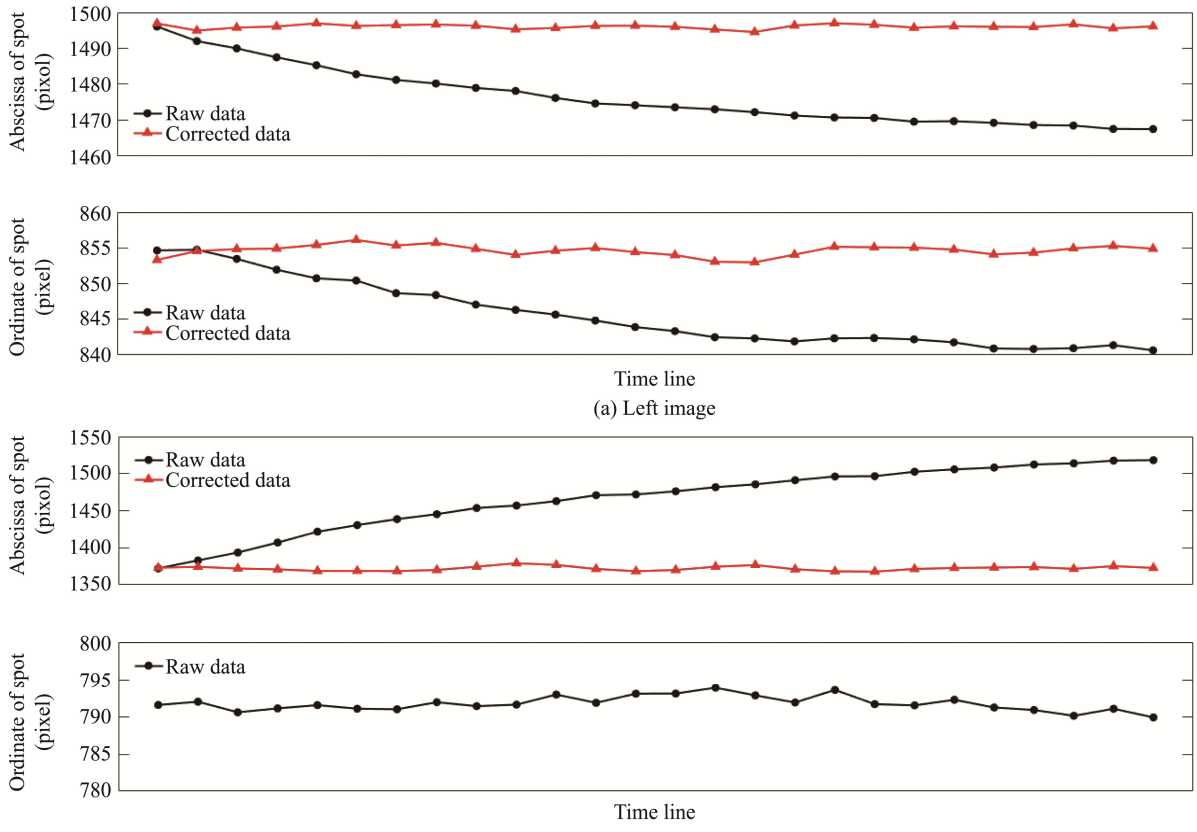

(a) Left image

(b) Right image (the ordinate of spot position is not corrected)

Fig.13 The result of environmental correction

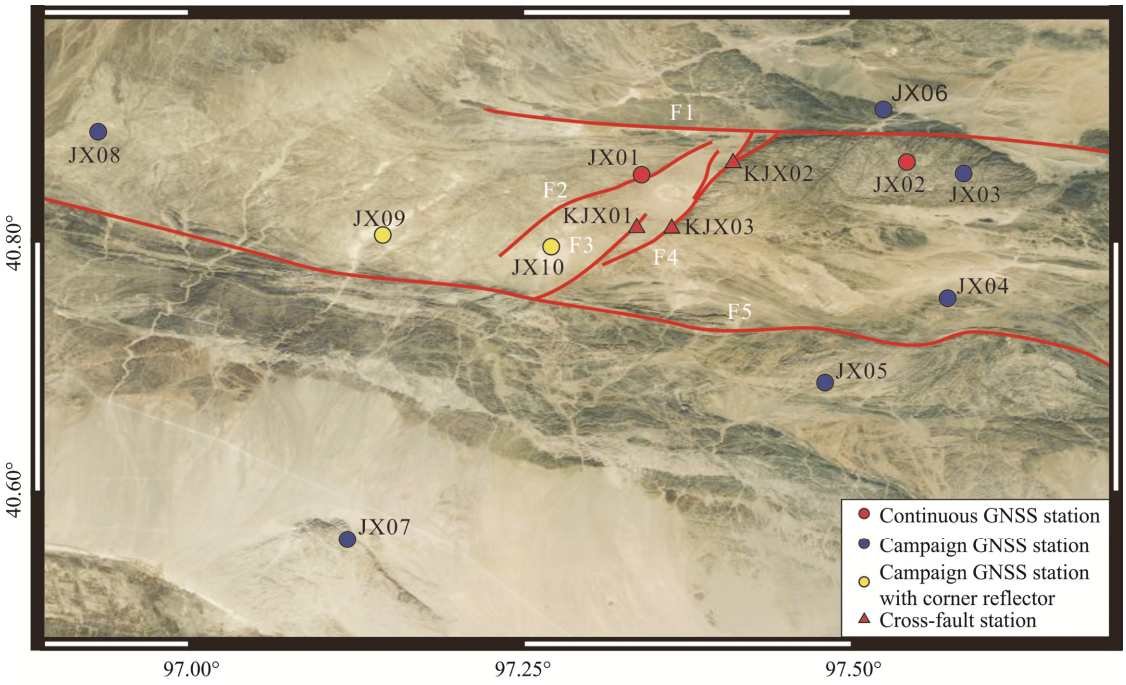

F1: Jinmiaogou fault; F2: Shiyuejing fault; F3: Jiujingxi fault; F4: Jiujing fault; F5: Hongqishan fault

Fig.14 The distribution of deformation monitoring stations around the Beishan URL

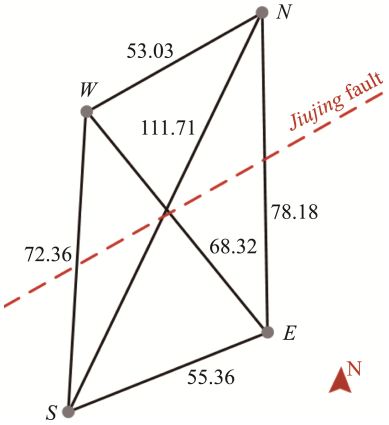

Fig.15 The site distribution of KJX02 (Unit: m)

Since *KJX02* is located in an uninhabited area without electricity supply, mobile communication and internet connection, the project proposes to collect monitoring data every 6 months, and conduct leveling and laser distance measurement at the same time; the verification of automatic monitoring data with leveling and laser distance data will be disclosed in the future work.

4 Conclusion and outlook

An automatic monitoring method for 3-D deformation of crustal faults based on laser and machine vision is proposed, and a prototype of an automatic monitoring system has been developed, which realizes a high sample rate of monitoring data with low cost compared with conventional techniques. The environmental correction model for temperature and humidity is determined to improve the system's stability under different environmental change. Long-term comparative experiment is underway at Beishan URL and more comparison reports will be revealed gradually, meanwhile, a remote management software based on the short message communication[23,24] of Beidou system (BDS) is being developed to enable the status and data stream of automatic monitoring system to be accessed remotely in real time.

Author Contributions:

WANG Qingshan: Conceptualization and writing original draft. SU Guoying: Data curation and resources. MA Qingzun: Project administration. YIN Haiquan: Data analysis and mapping. LIU Zhihang: Software programming and testing. LV Chuanzhen: Project investigations.

Fundings:

This work was supported by Earthquake Sciences Spark Programs of China Earthquake Administration (No. XH22020YA), Science Innovation Fund granted by the First Monitoring and Application Center of China Earthquake Administration (No. FMC202309).

Data Availability:

The authors declare that the main data supporting the findings of this study are available within the paper and its Supplementary Information files.

Conflict of Interest:

The authors declare no competing interests.

Dates:

Received 22 December 2023; Accepted 6 April 2024; Published online 30 June 2024

References

[1] Wu, Y. (2015). Crustal deformation before the 2008 Wenchuan M(S)8.0 earthquake studied using GPS data. Journal of Geodynamics. 85. pp.11-23.

[2] Zhang, G. (2023). Crustal deformations in the northeastern Tibetan Plateau revealed by multiple geodetic datasets. Pure and Applied Geophysics. 180. pp.703-714.

[3] Zhu, S. (2020). Inter- and pre-seismic deformations in the 2011 M-w 9. 0 Tohoku-Oki earthquake : Implications for earthquake prediction. *Chinese Journal of Geophysics-chinese Edition*. 63(2). pp.427-439.

[4] Wang, Q. (2020). A possible precursor prior to the Lushan earthquake from GPS observations in the southern Longmenshan. *Scientific Reports*. 10. pp.20833.

[5] Zhang, Y. (2022). The current crustal vertical deformation features of the Sichuan-Yunnan region constrained by fusing the leveling data with the GNSS data. *Remote Sensing*. 14(5). pp.1139.

[6] Rosen, P.A. (1996). Surface deformation and coherence measurements of Kilauea Volcano, Hawaii, from SIR-C radar interferometry. *Journal of Geophysical Research: Planets*. 101(E10). pp.23109-23125.

[7] Jing, C. (2022). GNSS/Accelerometer adaptive coupled landslide deformation monitoring technology. *Remote Sensing*. 14(15). pp.3537.

[8] Siaudinyte, L. (2016). Uncertainty evaluation of trigonometric method for vertical angle calibration of the total station instrument. *Measurement*. 86. pp.276-282.

Zhou, J. (2020). Automatic subway tunnel displacement monitoring using robotic total station. *Measurement*. 151. pp.107251.

[9] Ren, H. (2019). A review of UAV monitoring in mining areas: current status and future perspectives. *International Journal of Coal Science & Technology*. 6(3). pp.320-333.

[10] Cwiakala, P. (2020). UAV applications for determination of land deformations caused by underground mining. *Remote Sensing*. 12(11). pp.1733.

[11] Li, J. (2021). A health monitoring system for inverted arch of salt rock tunnel based on laser level deformation monitor and wFBG. *Measurement*. 184. pp.109909.

[12] Bornyakov, S.A. (2016). Instrumental deformation monitoring system and its trial in open-pit diamond mine. *Journal of Mining Science*. 52(2). pp.388-393.

[13] Muller, C. (2015). Integrated velocity field from ground and satellite geodetic techniques: application to Arenal volcano. *Geophysical Journal International*. 200(2). pp.861-877.

[14] Shang, X. (2020). Optical characteristics of the undamaged and laser damaged K9 glass in terahertz band. *Materials Research Express*. 7(4). pp.045202.

[15] Buades, A. (2011). Non-local means denoising. *Image Processing On Line*. 1. pp.208-212.

[16] LASEVER. (2023). A leading manufacturer for lasers. http://www.lasever.com.

[17] HIKROBOT. (2023). 5MP area scan camera. https://www.hikrobotics.com/en/machinevision/productdetail?id=5788.

[18] Wang, J. (2018). The Beishan underground research laboratory for geological disposal of high-level radioactive waste in China: Planning, site selection, site characterization and in situ tests. *Journal of Rock Mechanics and Geotechnical Engineering*. 10(3). pp.411-435.

[19] Ma, H. (2020). Excavation of underground research laboratory ramp in granite using tunnel boring machine: Feasibility study. *Journal of Rock Mechanics and Geotechnical Engineering*. 12(6). pp.1201-1213.

[20] Zhang, Y. (2020). Reliability analysis of deep underground research laboratory in Beishan for geological disposal of high-level radioactive waste. *Computers and Geotechnics*. 118. pp.103328.

[21] Zhang, Q. (2020). True three-dimensional geomechanical model tests for stability analysis of surrounding rock during the excavation of a deep underground laboratory. *Rock Mechanics and Rock Engineering*. 53(2). pp.517-537.

[22] Wang, W. (2015). On Beidou's Short Message Service-Based Data Transmission Solution. *Journal of Computational and Theoretical Nanoscience*. 12(9). pp.2556-2565.

[23] Li, G. (2021). Introduction to global short message communication service of BeiDou-3 navigation satellite system. *Advances in Space Research*. 67(5). pp.1701-1708.